

## Research Article

# CTAB-Assisted Hydrothermal Synthesis of WO<sub>3</sub> Hierarchical Porous Structures and Investigation of Their Sensing Properties

Dan Meng,<sup>1</sup> Guosheng Wang,<sup>1</sup> Xiaoguang San,<sup>1</sup> Yanbai Shen,<sup>2</sup> Guodong Zhao,<sup>1</sup> Yajing Zhang,<sup>1</sup> and Fanli Meng<sup>3</sup>

<sup>1</sup>College of Chemical Engineering, Shenyang University of Chemical Technology, Shenyang 110142, China

<sup>2</sup>College of Resources and Civil Engineering, Northeastern University, Shenyang 110819, China

<sup>3</sup>Research Center for Biomimetic Functional Materials and Sensing Devices, Institute of Intelligent Machines, Chinese Academy of Sciences, Hefei 230031, China

Correspondence should be addressed to Dan Meng; mengdan0610@hotmail.com and Fanli Meng; flmeng@iim.ac.cn

Received 27 August 2015; Accepted 19 October 2015

Academic Editor: Nguyen D. Hoa

Copyright © 2015 Dan Meng et al. This is an open access article distributed under the Creative Commons Attribution License, which permits unrestricted use, distribution, and reproduction in any medium, provided the original work is properly cited.

WO<sub>3</sub> hierarchical porous structures were successfully synthesized via cetyltrimethylammonium bromide- (CTAB-) assisted hydrothermal method. The structure and morphology were investigated using scanning electron microscope, X-ray diffractometer, transmission electron microscopy, X-ray photoelectron spectra, Brunauer-Emmett-Teller nitrogen adsorption-desorption, and thermogravimetry and differential thermal analysis. The result demonstrated that WO<sub>3</sub> hierarchical porous structures with an orthorhombic structure were constructed by a number of nanoparticles about 50–100 nm in diameters. The H<sub>2</sub> gas sensing measurements showed that well-defined WO<sub>3</sub> hierarchical porous structures with a large specific surface area exhibited the higher sensitivity compared with products without CTAB at all operating temperatures. Moreover, the reversible and fast response to H<sub>2</sub> gas and good selectivity were obtained. The results indicated that the WO<sub>3</sub> hierarchical porous structures are promising materials for gas sensors.

## 1. Introduction

Metal oxide semiconductors are widely used for the solar cells, photocatalysts, sensors, and so forth [1–4]. It is well known that the physical and chemical properties of most metal oxides are strongly dependent on their grain size, morphology, surface areas, and structure [5, 6]. Therefore, controlling these factors of the metal oxide materials is one of the most challenging issues in order to achieve reliable performance. Porous materials have attracted considerable attention because they have potentials in various promising applications owing to their higher specific area and an effective gas diffusion path via well-aligned porous structures [7–10]. Great efforts have been made to explore new synthesis methods and control the formation of porous structures to satisfy certain applications.

Tungsten oxide (WO<sub>3</sub>), an n-type semiconductor, has been widely investigated due to its unique optical and

electrical properties. Therefore, it is regarded as a promising materials for gas sensors, photocatalysts, electrode materials for secondary batteries, solar energy devices, and so forth [11–15]. For these applications, great interest arises in synthesis of high surface area WO<sub>3</sub> nano/micro-structures such as nanowires [16], nanoplates [17], and hierarchical architectures [18] to obtain enhanced performance. Recently, WO<sub>3</sub> porous structures with various morphologies have drawn extensive research attention since porous materials with high surface area usually exhibit unique chemical and physical properties different from solid structures, which make them critically important in technological applications [19]. Therefore, the controlling fabrication of ordered WO<sub>3</sub> porous structures through a facile, mild, and low cost method still has importantly scientific and practical significance.

In this paper, we reported a simple hydrothermal synthesis of WO<sub>3</sub> hierarchical porous structures constructed by nanoparticles, using sodium tungstate (Na<sub>2</sub>WO<sub>4</sub>·2H<sub>2</sub>O) as a

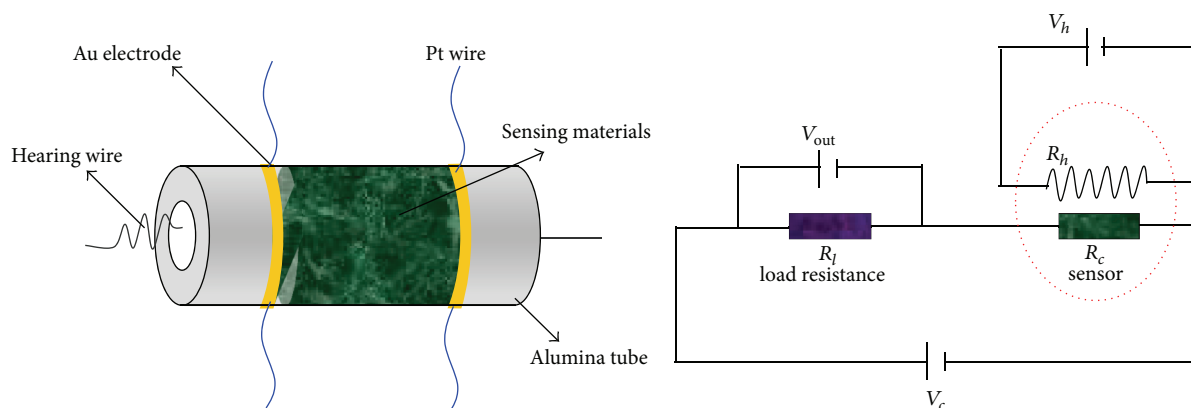


FIGURE 1: Schematic illustration of the gas sensor and measurement electric circuit ( $V_h$ : heating voltage,  $V_c$ : circuit voltage, and  $V_{out}$ : signal voltage).

tungsten source and CTAB as an assistant agent. The morphologies and structures and their  $H_2$  gas sensing properties were investigated. The result showed that the sensor fabricated from  $WO_3$  porous structures exhibited excellent  $H_2$  sensing properties, demonstrating potential of these unique hierarchical porous structures for gas sensor application.

## 2. Experimental

$WO_3$  hierarchical porous structures were synthesized by the hydrothermal method. In a typical procedure, 1.32 g  $Na_2WO_4 \cdot 2H_2O$  was dissolved in 20 mL distilled water under magnetic stirring to get a clear solution. Subsequently, 3 M HCl aqueous solution was slowly dropped into the solution under continuous stirring until the pH value of the solution reached 1. Then 0.8 g CTAB was added into the solution. After stirring 30 min, the mixture was transferred into a 50 mL Teflon-lined stainless autoclave with filling about 80% of the whole volume by mixing distilled water. The autoclave was maintained at  $180^\circ C$  for 12 h and then cooled down to room temperature naturally. The precipitate was collected and washed with distilled water and ethanol for three times, respectively, and dried in an oven at  $80^\circ C$  for 4 h. To observe the effect of CTAB, the product without assistance of CTAB was synthesized maintaining the same condition. Finally, the products were annealed at  $400^\circ C$  in air for 4 h for investigating the crystal structure, morphology, and gas sensing properties. The final product without assistance of CTAB was named as SW, while that with assistance of CTAB was named as SW-CTAB.

The obtained products were characterized using an X-ray diffractometer (XRD, PANalytical X'Pert Pro), a field emission scanning electron microscope (FESEM, ZEISS Ultra Plus) equipped with energy dispersive X-ray spectroscopy (EDS), a transmission electron microscopy (TEM-JEOL EM002B), an X-ray photoelectron spectra (XPS, JEOL JPS9010MC), and Brunauer-Emmett-Teller (BET) nitrogen adsorption-desorption (TristarII3020M). The pore size distribution was calculated from the adsorption branch of the nitrogen adsorption-desorption isotherms using the Barrett-Joyner-Halenda (BJH) method. Thermogravimetry and

differential thermal analysis (TG-DTA) was also carried out using a Shimadzu, DTG-60H apparatus. The sample was heated from room temperature to  $800^\circ C$  at a rate of  $10^\circ C/min$  in air.

In order to prepare gas sensors, the obtained products were mixed with ethanol to form a paste, which was then coated onto the outside surface of an alumina tube with a pair of Au electrodes and four Pt wires. A Ni-Cr alloy coil inserted into the tube was used as heater; the temperature of coated tube could be controlled by regulating heating voltage. Then, the sensors were annealed at  $350^\circ C$  for 4 h in ambient air to improve their stability and repeatability. The gas sensing measurements were performed on a static system (WS-30A, Hanwei Electronics Co. Ltd., Henan Province, China) with the constant loop voltage of 5 V. Figure 1 shows the schematic diagrams of the sensor and measurement electric circuit. The sensitivity of the sensor is defined as the ratio of the electrical resistance in air ( $R_a$ ) to the electrical resistance in the mixture of test gas and air ( $R_g$ ), which is given by the equation  $S = R_a/R_g$ .

## 3. Results and Discussion

**3.1. Structure Characterizations.** Figure 2 shows the TG-DTA curves of the nonannealed SW-CTAB product. It is found that the total weight loss is only 1.1% from room temperature to  $400^\circ C$ , which is attributed to the loss of surface adsorbed water and the combustion of the organics adsorbed on the surface of the product. There was no obvious weight loss between  $400^\circ C$  and  $800^\circ C$ , indicating that all the organics were completely removed. A broad exothermic peak between  $400^\circ C$  and  $800^\circ C$  of the DTA curve is associated with the further crystallization of  $WO_3$  [20]. Thus, the annealing temperature for the product was set at the  $400^\circ C$  to maintain the porous structure.

The XRD patterns observed for the SW and SW-CTAB products are shown in Figure 3. It is clearly seen that all the diffraction peaks of two products are in good agreement with JCPDS cards 71-0131, which could be indexed to orthorhombic crystal structure. The peaks of other impurity phases were not observed in the XRD patterns, indicating the obtained

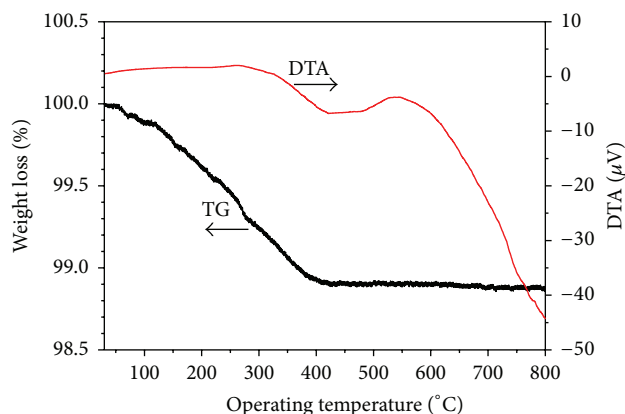


FIGURE 2: TG and DTA curves of the nonannealed SW-CTAB product.

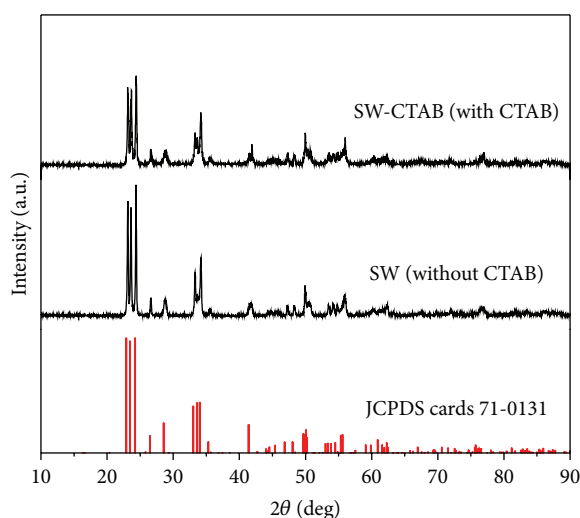


FIGURE 3: XRD patterns of the SW and SW-CTAB products.

products are pure  $\text{WO}_3$  structures under the hydrothermal conditions. The strong and sharp diffraction peaks indicate the good crystallinity of the products.

FESEM images of the SW and SW-CTAB products are shown in Figures 4(a)–4(e). Figures 4(a) and 4(b) indicate that SW products are composed of particles with heterogeneous morphology in shape of irregular sphere-like structures and plate-like structures. The size of sphere-like structures is approximately 20–100 nm, while the size of plate-like structures is approximately 50 nm in thickness and 100–500 nm in length. It is interesting that the morphologies of the SW-CTAB products vary dramatically, showing porous structures (Figure 4(c)). Many large pores with around 1–3  $\mu\text{m}$  are observed. The high-magnification FESEM image, as shown in Figure 4(d), reveals that these porous structures consisted of interconnected spherical nanoparticles, which are self-assembled layer by layer and the large pores are bound between the big particles. Carefully observation in Figures 4(e) and 4(f) demonstrates that the particle diameter is in the range of 50–100 nm. The irregular pores and unambiguous grain boundaries between the nanoparticles are obviously

observed. The EDS spectrum for the SW and SW-CTAB products shown in Figures 4(g) and 4(h), respectively, indicate that only oxygen and tungsten elements exist in two products with an atomic ratio of nearly 3 : 1.

The above observations indicate that the presence of CTAB is favorable for forming  $\text{WO}_3$  porous structures. CTAB is a cationic surfactant, which is suitable for scattering, self-assembly and pore-making [21–24]. In the present work, the reason for the formation of the hierarchical porous architectures is most likely due to the interaction between CTAB molecular layers adsorbed on the particle surface and oriented aggregation of nanocrystals. Initially, the tungstate acid ( $\text{H}_2\text{WO}_4 \cdot n\text{H}_2\text{O}$ ) was formed rapidly and precipitated from solution after HCl solution was added dropwise into  $\text{Na}_2\text{WO}_4$  solution (shown in formula (1)). When CTAB was introduced into aqueous solution, CTAB molecules could adsorb on the surfaces of  $\text{H}_2\text{WO}_4 \cdot n\text{H}_2\text{O}$  tiny particles. During the continuous hydrothermal process, these tiny particles in the presence of CTAB could dissolve, decompose into different shapes of  $\text{WO}_3$  nuclei, and regrow to nanoparticles through Ostwald ripening process [24]. In this process, the

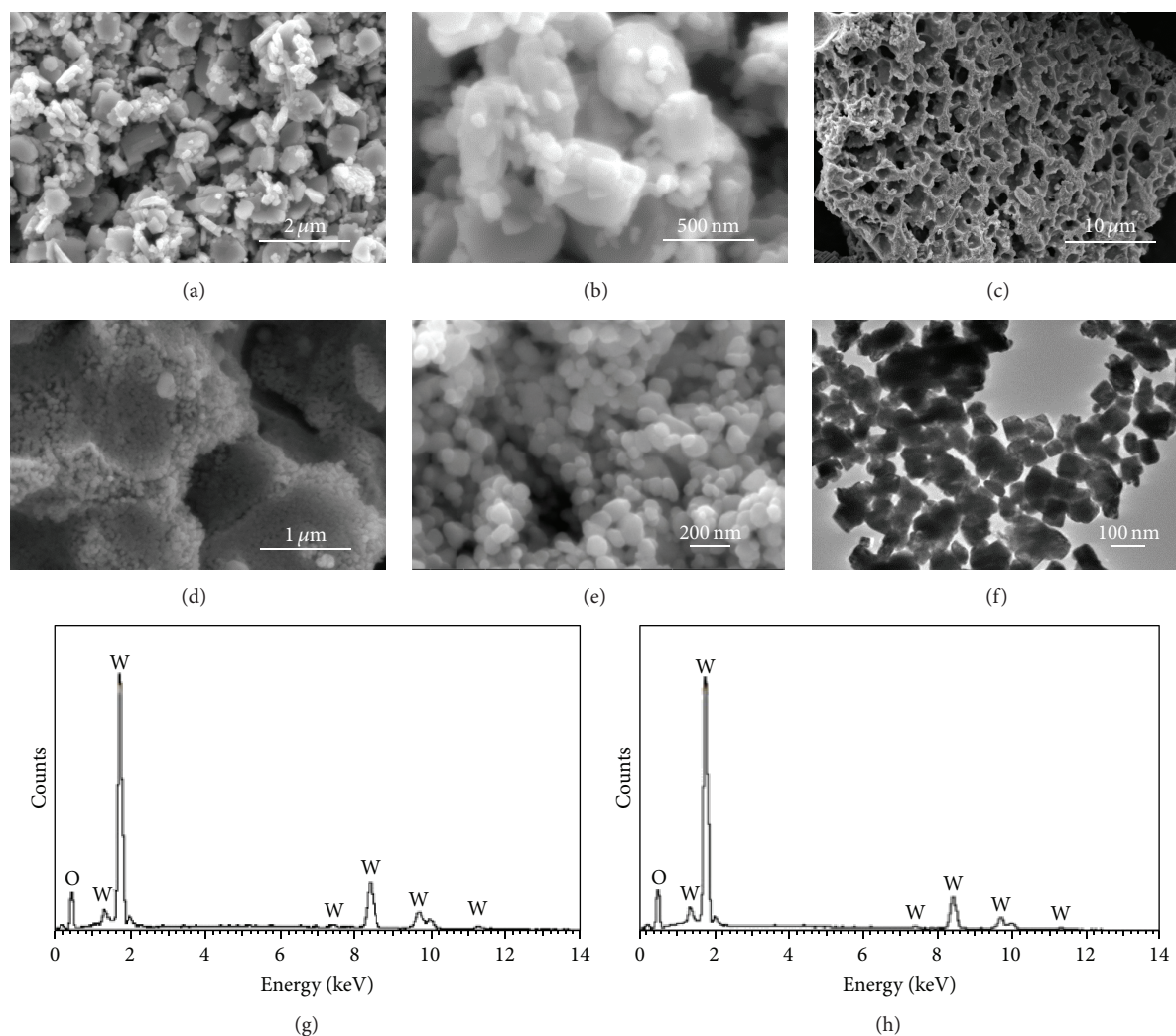
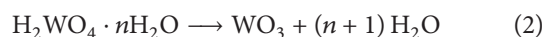


FIGURE 4: (a)–(e) FESEM images and EDS pattern of the SW and SW-CTAB products: (a) and (b) FESEM images of the SW product, (c)–(e) FESEM images of the SW-CTAB product. (f) TEM image of the SW-CTAB product, (g) and (h) EDS pattern of the SW product and SW-CTAB product, respectively.

adsorption of CTAB on crystal planes may account for the inhibition of the epitaxy growth of the particles and thus the formation of small sizes nanoparticles. As the reaction went on, these nanoparticles further oriented aggregate with each other to minimize the total surface free energy of the system [25]. The reaction in the solution can be shown below [23, 24]:



The nitrogen adsorption-desorption measurement isotherm and pore size distribution as the inset of the SW and SW-CTAB products are shown in Figure 5. According to the IUPAC classification, both SW and SW-CTAB products exhibit type IV form with a type H3 hysteresis loop. The type H3 loops appear at the relative pressure ( $P/P_0$ ) range of 0.8–1.0 and indicated that the pore size is relatively large. The pore size distributions of both SW and SW-CTAB products

distribute in the long range of 2–110 nm. The BET surface of SW-CTAB product is  $28.3 \text{ m}^2 \text{ g}^{-1}$ , which is higher than that of SW product ( $4.5 \text{ m}^2 \text{ g}^{-1}$ ).

The typical XPS spectrum for the SW-CTAB product is shown in Figure 6. Wide scanning spectrum in Figure 6(a) indicates that the W, O, and C are present in the product and no other impurities are found. Elements W and O belong to the  $\text{WO}_3$  product and C may be attributed to the sample handling and exposure to the atmosphere prior to XPS measurements. Narrow scan XPS spectra of W 4f and O 1s are shown in Figures 6(b) and 6(c). The well-resolved W 4f doublet peaks are due to spin orbit coupling of electrons. Peaks locating at 35.46 and 37.58 eV correspond to W 4f<sub>7/2</sub> and W 4f<sub>5/2</sub>, respectively, agreeing well with the  $\text{W}^{6+}$  state from  $\text{WO}_3$ . The O 1s peak at 529.81 eV corresponds to the lattice oxygen  $\text{O}^{2-}$  bonded to W. The above observation demonstrates that the product is close to the chemical stoichiometry of  $\text{WO}_3$  [22, 26].

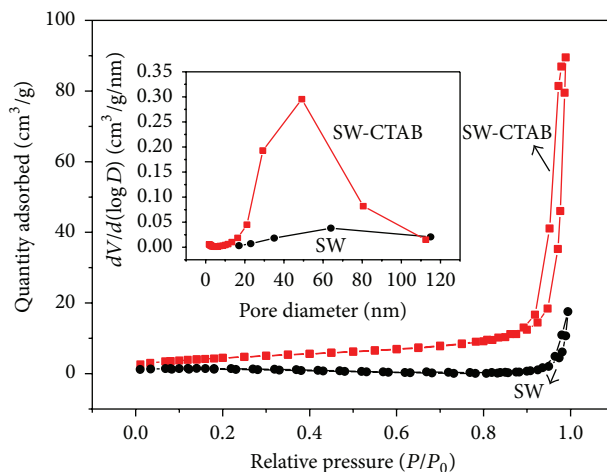


FIGURE 5: Nitrogen adsorption-desorption measurement isotherm and the corresponding pore size distribution (inset) of the SW and SW-CTAB products.

**3.2. Sensing Properties of  $H_2$ .** Consider that the  $WO_3$  hierarchical porous structures possess a large active surface area and fast gas diffusion, which are beneficial for gas sensor, photochemical device, and catalysis applications. Here, the  $H_2$  sensing properties were investigated.

The sensitivity of the sensors made of SW and SW-CTAB products upon exposure to 1000 ppm  $H_2$  gas is shown in Figure 7 as a function of the operating temperature. It is obvious that their sensing response largely depend on operating temperature. The highest sensitivity for the SW product is 12.8 at  $300^\circ C$ , while it is 26.2 for SW-CTAB product at  $250^\circ C$ . In addition, the sensor made of hierarchical porous structures obtained with CTAB exhibits the higher sensitivity to  $H_2$  gas at almost all the operating temperatures, indicating that the porous structures with many pores and intervals are very good candidate for gas sensor.

The temporal responses of the sensors made of SW and SW-CTAB products upon exposure to 1000 ppm  $H_2$  gas at different operating temperatures are shown in Figure 8. The resistance of both sensors decreases rapidly upon exposure to  $H_2$  gas and quickly recovers to its initial value when gas is out, at high temperature of  $300^\circ C$ . However, response and recovery rate are slow at a low temperature, especially for the SW product, and the resistant can not recover to the initial value at  $100^\circ C$ . Here, the response time and recovery time are defined as the time required for the resistance to reach 90% of the equilibrium value after detected gas is introduced, and the time necessary for the sensor to recover 90% of its initial resistance, respectively. With increasing the temperature, the response time and response time for the sensor made of SW-CTAB product range from 136 to 18 s and 920 to 76 s, respectively, while they range from 176 to 56 s and 1020 to 104 s, respectively, for the sensor made of SW product. Such result suggests that the sensor based on porous structures exhibits quicker response and recover characteristics, indicating the good response and recover performance.

The gas response and recovery behavior of the sensor upon exposure to different concentration  $H_2$  (500–10000 ppm) at  $250^\circ C$  are shown in Figures 9(a) and 9(b). It is can be seen that both sensors exhibit good response/recovery characteristics to  $H_2$  gas pulses at different concentrations, indicating excellent reversibility and stability of the sensors. Moreover, the response and recovery rate of the SW-CTAB product are faster than those of the SW product, which can be ascribed to the hierarchical porous structures. The sensitivity as a function of  $H_2$  concentration is shown in Figure 9(c). It is noted that the sensitivity increases as  $H_2$  concentration increases for both sensors. In addition, the sensor made of the SW-CTAB product shows the higher sensitivity than the sensor made of the SW product at all  $H_2$  concentrations.

Gas sensing responses of the sensors made of  $WO_3$  porous structures obtained with CTAB assistant to different volatile gases under concentration of 100 ppm at  $250^\circ C$  were measured, as shown in Figure 10. It clearly shows that the sensor is more sensitive to 1000 ppm  $H_2$  than to other interference gases, implying that selective detecting of  $H_2$  is possible.

$WO_3$  is a typical n-type semiconductor. Its gas sensing mechanism belongs to the surface-controlled type, and the change of resistance is dependent on the species and the amount of chemisorbed species on the surface [11]. A possible sensing mechanism is proposed in Figure 11. The oxygen molecules from the ambient atmosphere are initially adsorbed on the surface of the  $WO_3$  grain in the form of  $O_2^-$ ,  $O^-$ , and  $O^{2-}$ , depending on the ambient temperature [27]. Thus, every  $WO_3$  particle has a depletion layer near its surface, and many boundaries are formed between particles, leading to high resistance state in air ambient. When  $WO_3$  are exposed to a reducing gas such as hydrogen, these gas molecules could react with surface oxygen species by  $H_2(gas) + 1/2O_2^-(ads) \rightarrow H_2O(ads) + e^-$  and  $H_2(gas) + O^-(ads) \rightarrow H_2O(ads) + e^-$  [28]. This process releases the electrons back to

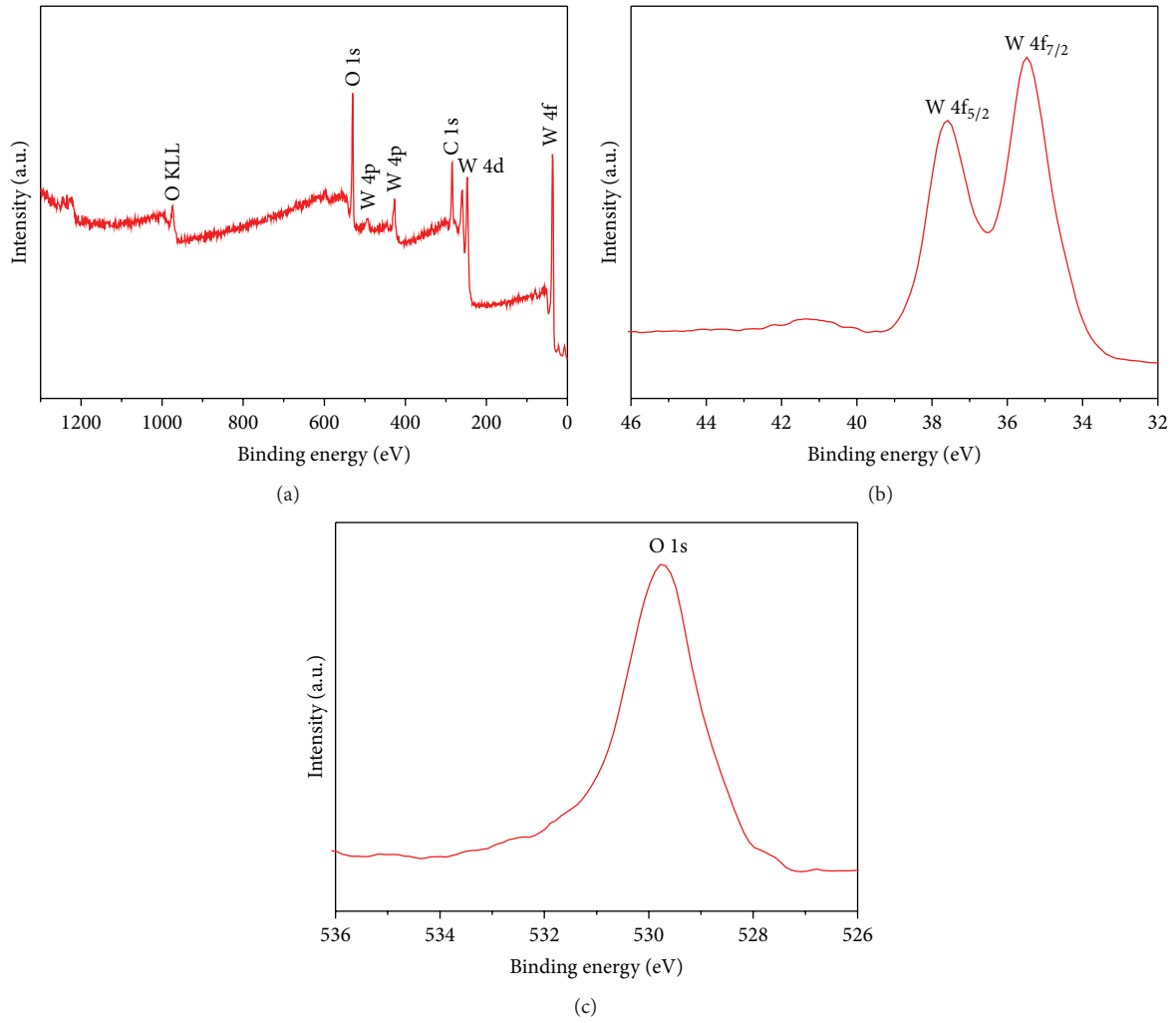


FIGURE 6: XPS spectrum for the SW-CTAB product: (a) wide scan spectrum, (b) W 4f spectra, and (c) O 1s spectra.

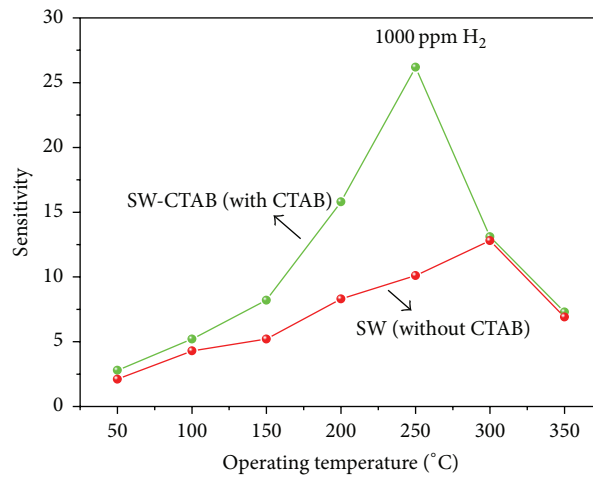


FIGURE 7: Sensitivity upon exposure to 1000 ppm H<sub>2</sub> gas at different operating temperatures.

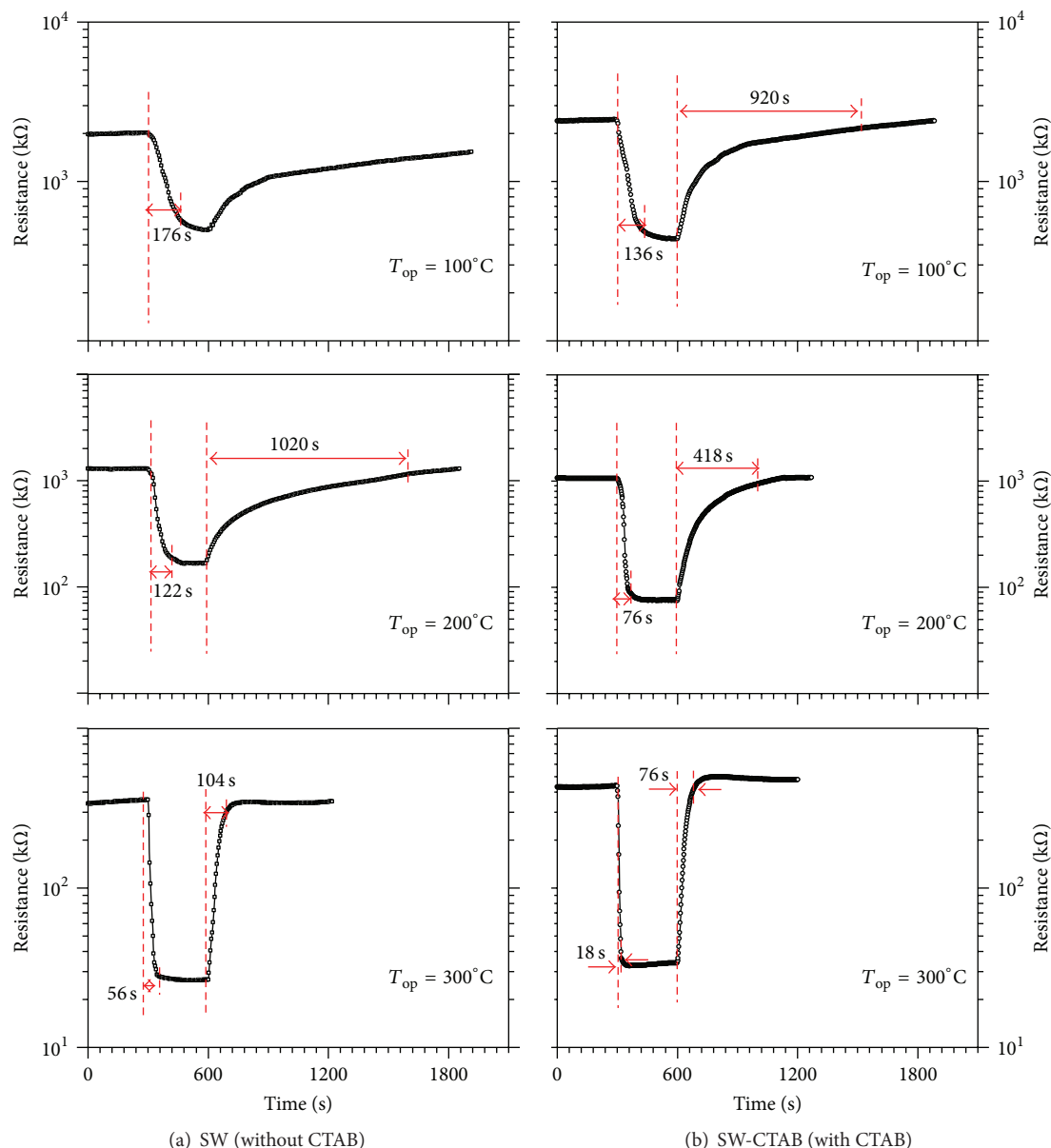


FIGURE 8: Temporal responses upon exposure to 1000 ppm  $\text{H}_2$  gas at different operating temperatures. (a) SW (without CTAB) and (b) SW-CTAB (with CTAB).

$\text{WO}_3$  and barrier height at the grain boundaries decreases. As a result, the resistance of  $\text{WO}_3$  particles decreases, reflecting a sensing property. The hierarchical porous structures with a large surface and high porosity may enhance the probability of absorbing target gases and providing an effective gas diffusion path via well-aligned porous structures. Therefore, the  $\text{WO}_3$  hierarchical porous structure sensor exhibits excellent sensing properties.

#### 4. Conclusions

In summary, high-performance  $\text{WO}_3$  hierarchical porous structures were synthesized by hydrothermal process via CTAB as surfactant. These  $\text{WO}_3$  porous structures with an orthorhombic structure were constructed by a number of

nanoparticles about 50–100 nm in diameters. The  $\text{H}_2$  gas sensing properties were investigated. The result demonstrated that well-defined  $\text{WO}_3$  hierarchical porous structures with large specific surface area exhibited the higher responses compared with products without CTAB at all operating temperatures. Moreover, the reversible and fast response to  $\text{H}_2$  gas and good selectivity were obtained. These excellent sensing properties of  $\text{WO}_3$  hierarchical porous structures indicate a potential application for fabrication high-performance gas sensors.

#### Conflict of Interests

The authors declare that there is no conflict of interest regarding the publication of this paper.

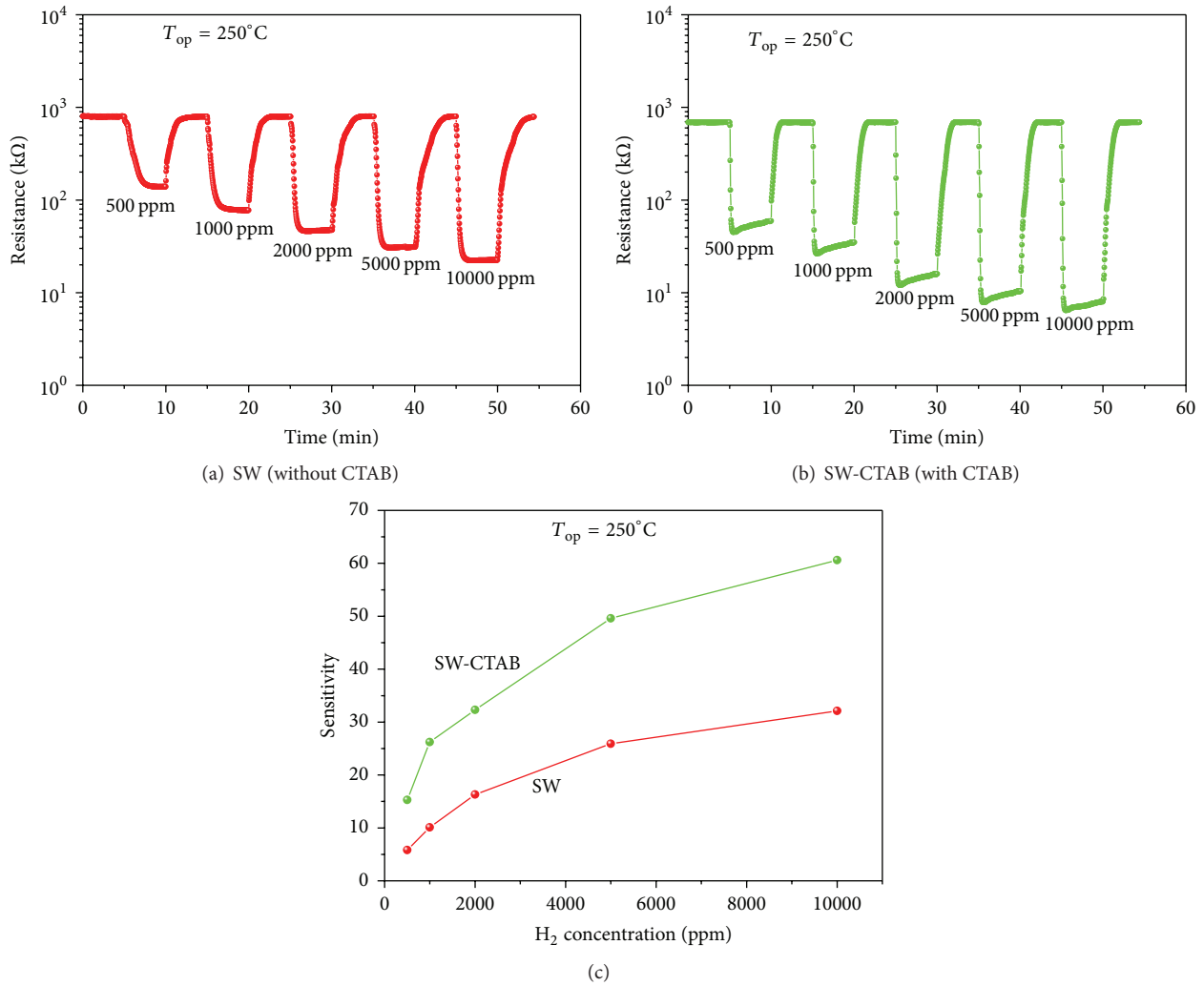


FIGURE 9: Temporal responses upon exposure to 500–10000 ppm  $\text{H}_2$  gas measured at  $250^\circ\text{C}$ . (a) SW (without CTAB) and (b) SW-CTAB (with CTAB). (c) Relationship between the sensitivity and  $\text{H}_2$  concentration at  $250^\circ\text{C}$ .

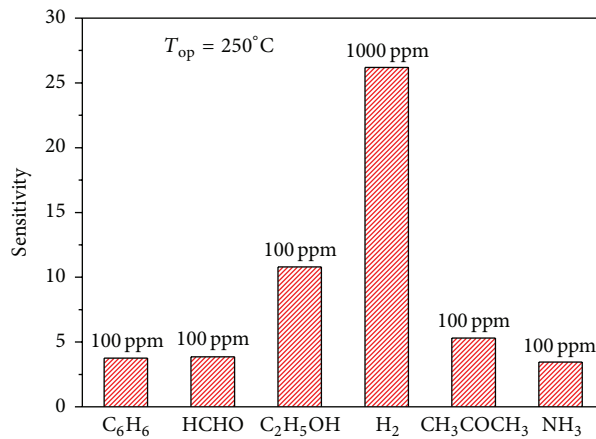


FIGURE 10: Selectivity of the sensor made of the SW-CTAB product exposure to different gases at  $250^\circ\text{C}$ . Here, the concentration of volatile gases is 100 ppm, while it is 1000 ppm for  $\text{H}_2$  gas.

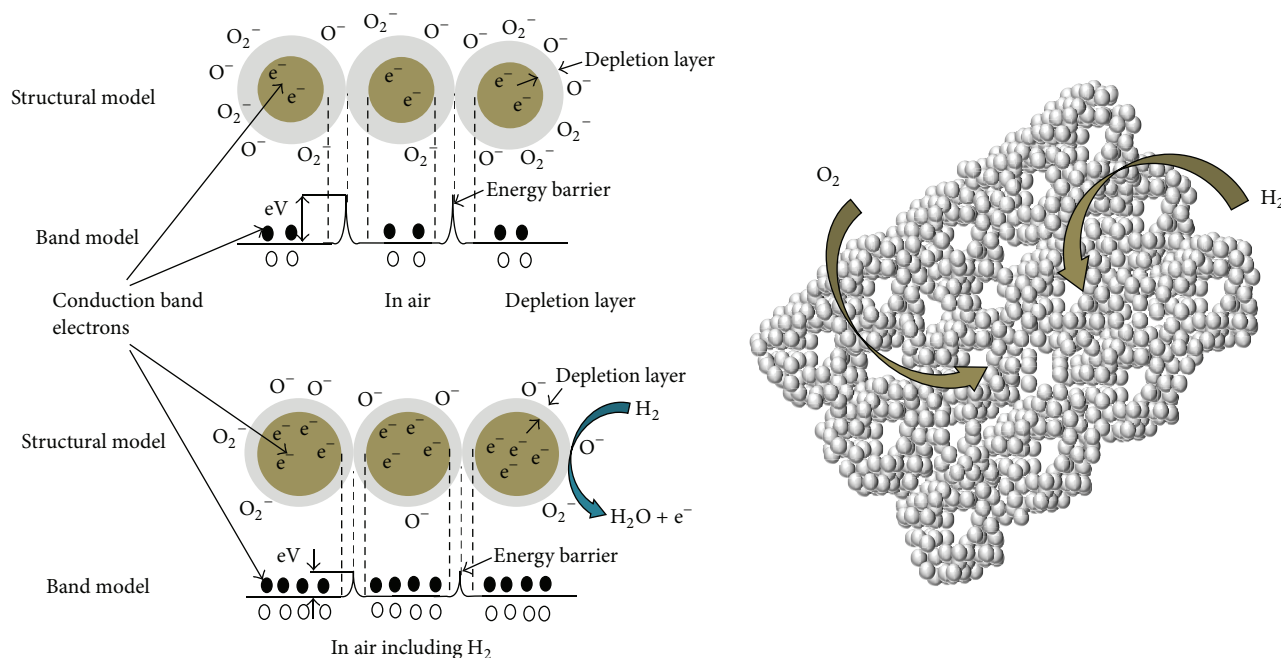


FIGURE 11: Schematic illustration of gas sensing mechanism.

## Acknowledgments

The authors are grateful for the support of the National Natural Science Foundation of China (nos. 61403263, 61374017, 51422402, 51301114, and 21503137) and Liaoning Educational Department Foundation (no. L2014167).

## References

- [1] S. H. Ko, D. Lee, H. W. Kang et al., "Nanoforest of hydrothermally grown hierarchical ZnO nanowires for a high efficiency dye-sensitized solar cell," *Nano Letters*, vol. 11, no. 2, pp. 666–671, 2011.
- [2] J. C. Chen and J. Q. Xu, "SnO<sub>2</sub>-based R134a gas sensor: sensing materials preparation, gas response and sensing mechanism," *Sensors and Actuators B: Chemical*, vol. 157, no. 2, pp. 494–499, 2011.
- [3] S. Sun, J. J. Ding, J. Bao et al., "Photocatalytic degradation of gaseous toluene on Fe-TiO<sub>2</sub> under visible light irradiation: a study on the structure, activity and deactivation mechanism," *Applied Surface Science*, vol. 258, no. 12, pp. 5031–5037, 2012.
- [4] M. Laurenti, N. Garino, S. Porro, M. Fontana, and C. Gerbaldi, "Zinc oxide nanostructures by chemical vapour deposition as anodes for Li-ion batteries," *Journal of Alloys and Compounds*, vol. 640, pp. 321–326, 2015.
- [5] T.-D. Nguyen, C.-T. Dinh, and T.-O. Do, "A general procedure to synthesize highly crystalline metal oxide and mixed oxide nanocrystals in aqueous medium and photocatalytic activity of metal/oxide nanohybrids," *Nanoscale*, vol. 3, no. 4, pp. 1861–1873, 2011.
- [6] G. Korotcenkov, "The role of morphology and crystallographic structure of metal oxides in response of conductometric-type gas sensors," *Materials Science & Engineering R: Reports*, vol. 61, no. 1–6, pp. 1–39, 2008.
- [7] B. Hu, C. Xiong, K. Tao, and S. Zhou, "Metathesis of 1-butene and ethene to propene over mesoporous W-KIT-6 catalysts: the influence of Si/W ratio," *Journal of Porous Materials*, vol. 22, no. 3, pp. 613–620, 2015.
- [8] Q. Jin, Z. Li, K. Lin, S. Wang, R. Xu, and D. Wang, "Synthesis of a hierarchically meso-macroporous TiO<sub>2</sub> film based on UV light-induced in situ polymerization: application to dye-sensitized solar cells," *RSC Advances*, vol. 4, no. 84, pp. 44692–44699, 2014.
- [9] N. D. Hoa, N. V. Duy, S. A. El-Safty, and N. V. Hieu, "Meso-/nanoporous semiconducting metal oxides for gas sensor applications," *Journal of Nanomaterials*, vol. 2015, Article ID 972025, 14 pages, 2015.
- [10] J. R. Huang, L. Y. Wang, C. P. Gu, Z. J. Wang, Y. F. Sun, and J.-J. Shim, "Preparation of porous SnO<sub>2</sub> microcubes and their enhanced gas-sensing property," *Sensors and Actuators B: Chemical*, vol. 207, pp. 782–790, 2015.
- [11] H. W. Long, W. Zeng, and H. Zhang, "Synthesis of WO<sub>3</sub> and its gas sensing: a review," *Journal of Materials Science: Materials in Electronics*, vol. 26, no. 7, pp. 4698–4707, 2015.
- [12] H. Simchi, B. E. McCandless, T. Meng, and W. N. Shafarman, "Structural, optical, and surface properties of WO<sub>3</sub> thin films for solar cells," *Journal of Alloys and Compounds*, vol. 617, pp. 609–615, 2014.
- [13] S. S. Thind, M. Tian, and A. Chen, "Direct growth and photoelectrochemical study of WO<sub>3</sub> nanostructured materials," *Electrochemistry Communications*, vol. 43, pp. 13–17, 2014.
- [14] A. B. D. Nandiyanto, O. Arutanti, T. Ogi, F. Iskandar, T. O. Kim, and K. Okuyama, "Synthesis of spherical macroporous WO<sub>3</sub> particles and their high photocatalytic performance," *Chemical Engineering Science*, vol. 101, pp. 523–532, 2013.
- [15] X. C. Duan, S. H. Xiao, L. L. Wang et al., "Ionic liquid-modulated preparation of hexagonal tungsten trioxide mesocrystals for lithium-ion batteries," *Nanoscale*, vol. 7, no. 6, pp. 2230–2234, 2015.

- [16] W. Zeng, B. Miao, T. F. Li et al., "Hydrothermal synthesis, characterization of h-WO<sub>3</sub> nanowires and gas sensing of thin film sensor based on this powder," *Thin Solid Films*, vol. 584, pp. 294–294, 2015.
- [17] W.-H. Hu, G.-Q. Han, B. Dong, and C.-G. Liu, "Facile synthesis of highly dispersed WO<sub>3</sub>·H<sub>2</sub>O and WO<sub>3</sub> Nanoplates for Electrocatalytic Hydrogen Evolution," *Journal of Nanomaterials*, vol. 2015, Article ID 346086, 6 pages, 2015.
- [18] C. Wang, X. Li, C. H. Feng, Y. F. Sun, and G. Y. Lu, "Nanosheets assembled hierarchical flower-like WO<sub>3</sub> nanostructures: synthesis, characterization, and their gas sensing properties," *Sensors and Actuators B: Chemical*, vol. 210, pp. 75–81, 2015.
- [19] J. Zeng, M. Hu, W. D. Wang, H. Q. Chen, and Y. X. Qin, "NO<sub>2</sub>-sensing properties of porous WO<sub>3</sub> gas sensor based on anodized sputtered tungsten thin film," *Sensors and Actuators B: Chemical*, vol. 161, no. 1, pp. 447–452, 2012.
- [20] H. Zheng, J. Z. Ou, M. S. Strano, R. B. Kaner, A. Mitchell, and K. Kalantar-Zadeh, "Nanostructured tungsten oxide—properties, synthesis, and applications," *Advanced Functional Materials*, vol. 21, no. 12, pp. 2175–2196, 2011.
- [21] Y. Q. Wang, R. M. Cheng, Z. Wen, and L. J. Zhao, "Facile preparation of Fe<sub>3</sub>O<sub>4</sub> nanoparticles with cetyltrimethylammonium bromide (CTAB) assistant and a study of its adsorption capacity," *Chemical Engineering Journal*, vol. 181-182, pp. 823–827, 2012.
- [22] N. Asim, S. Radiman, and M. A. B. Yarmo, "Synthesis of WO<sub>3</sub> in nanoscale with the usage of sucrose ester microemulsion and CTAB micelle solution," *Materials Letters*, vol. 61, no. 13, pp. 2652–2657, 2007.
- [23] Y.-X. Wang, J. Sun, X. Y. Fan, and X. Yu, "A CTAB-assisted hydrothermal and solvothermal synthesis of ZnO nanopowders," *Ceramics International*, vol. 37, no. 8, pp. 3431–3436, 2011.
- [24] D. Sánchez-Martínez, C. Gómez-Solís, and L. M. Torres-Martínez, "CTAB-assisted ultrasonic synthesis, characterization and photocatalytic properties of WO<sub>3</sub>," *Materials Research Bulletin*, vol. 61, pp. 165–172, 2015.
- [25] M. Y. Zhu, D. H. Meng, C. J. Wang, and G. W. Diao, "Facile fabrication of hierarchically porous CuFe<sub>2</sub>O<sub>4</sub> nanospheres with enhanced capacitance property," *ACS Applied Materials & Interfaces*, vol. 5, no. 13, pp. 6030–6037, 2013.
- [26] C. W. Song, C. Li, Y. Y. Yin et al., "Preparation and gas sensing properties of partially broken WO<sub>3</sub> nanotubes," *Vacuum*, vol. 114, pp. 13–16, 2015.
- [27] M. Bekri, N. M. Shaalan, and A. S. Ahmed, "Thermal evaporated WO<sub>3</sub> nanoparticles film under different evaporation pressures for NO<sub>2</sub> sensing," *Digest Journal of Nanomaterials and Biostructures*, vol. 10, no. 2, pp. 603–613, 2015.
- [28] W. Chomkitichai, H. Ninsonthi, C. Liewhiran, A. Wisitsoraat, S. Sriwichai, and S. Phanichphant, "Flame-made Pt-loaded TiO<sub>2</sub> thin films and their application as H<sub>2</sub> gas sensors," *Journal of Nanomaterials*, vol. 2013, Article ID 497318, 8 pages, 2013.



**Hindawi**

Submit your manuscripts at  
<http://www.hindawi.com>

